ACS NANO

Article

Suppressing the Shuttle Effect and Dendrite Growth in Lithium-Sulfur Batteries

Jianan Wang, Shanshan Yi, Jianwei Liu, Sun Shiyi, Yunpeng Liu, Duowen Yang, Kai Xi, Guoxin Gao, Amr Abdelkader, Wei Yan, Shujiang Ding, and Ramachandran Vasant Kumar

ACS Nano, **Just Accepted Manuscript** • DOI: 10.1021/acsnano.0c02241 • Publication Date (Web): 07 Jul 2020

Suppressing the Shuttle Effect and Dendrite Growth in Lithium-Sulfur Batteries

Jianan Wang,[†,§] Shanshan Yi,[†] Jianwei Liu,[†] Shiyi Sun,[†] Yunpeng Liu,[†] Duowen Yang,[†] Kai Xi,*[,‡,ǁ] Guoxin Gao,[†,§] Amr Abdelkader,[Γ] Wei Yan,*[,†,§] Shujiang Ding,*[,†,§] and Ramachandran Vasant Kumar[ǁ]

[†]Department of Environmental Science and Engineering, Department of Applied Chemistry, School of Chemistry, MOE Key Laboratory for Nonequilibrium Synthesis and Modulation of Condensed Matter, State Key Laboratory for Electrical Insulation and Power Equipment, Xi'an Jiaotong University, Xi'an 710049, China.

[‡]Department of Engineering, University of Cambridge, Cambridge, CB3 0FA, United Kingdom.

[ǁ]Department of Materials Science and Metallurgy, University of Cambridge, Cambridge, CB3 0FS, United Kingdom.

[Γ]Faculty of Science and Technology, Bournemouth University, Talbot Campus, Fern Barrow, Poole, BH12 5BB, United Kingdom.

[§]Xi'an Jiaotong University & Shaanxi Quantong Joint Research Institute of New Energy Vehicles Power

*E-mail: dingsj@xjtu.edu.cn (S. Ding); yanwei@xjtu.edu.cn (W. Yan); kx210@cam.ac.uk (K. Xi)

ABSTRACT: Practical applications of lithium-sulfur batteries are simultaneously hindered by two serious problems occurring separately in both electrodes, namely, the shuttle effects of lithium polysulfides and the uncontrollable growth of lithium dendrites. Herein, to explore a facile integrated approach to tackle both problems as well as guarantee the efficient charge transfer, we used two-dimension hexagonal VS_2 flakes as the building blocks to assemble nanotowers on the separators, forming symmetrical double-side-modified polypropylene separator without blocking the membrane pores. Benefiting from the "sulfiphilic" and "lithiophilic" properties, high interfacial electronic conductivity and unique hexagonal tower-form nanostructure, the D-HVS@PP separator not only guarantee the effective suppression of lithium polysulfide shuttle and the rapid ion/electron transfer, but also realize the uniform and stable lithium nucleation and growth during cycling. Hence, just at the expense of an 11% increase in the separator weight (0.14 mg cm^{-2}), D-HVS@PP separator delivers an over 16 times higher initial areal capacity (8.3 mAh cm^{-2}) than conventional PP separator (0.5 mAh cm^{-2}) under high sulfur-loading condition (9.24 mg cm^{-2}). Even when used under a low electrolyte/sulfur ratio of 4 mL g^{-1} and a practically relevant N/P ratio of 1.7, D-HVS@PP separator still enabled stable cycling with a high cell-level gravimetric energy density. The potentials in broader applications (Li-S pouch battery and Li-$LiFePO_4$ battery) and the promising commercial prospect (large-scale production and recyclability) of the developed separator are also demonstrated.

KEYWORDS: *lithium-sulfur batteries, amphiphilic, separator, lithium dendrites, recyclable, shuttle effect*

The rapid development of portable electronic devices, electric vehicles and smart grids has evoked the ever-increasing demand for high-energy-density energy storage systems with sustainable electrochemical performances.[1-3] Lithium-sulfur (Li-S) batteries are regarded as a potential alternative to current state-of-the-art Li-ion batteries owing to their high theoretical capacity (1675 mAh g^{-1} of sulfur) and energy density (2600 Wh kg^{-1}), low cost and environmental friendliness.[4-6] Despite such a bright perspective, the practical implementation of Li-S batteries is still facing some tough challenges. In terms of the sulfur cathode, the severe "shuttling effect" of the dissolved intermediate lithium polysulfides (Li_2S_x) gives rise to low active sulfur utilization, low coulombic efficiency and rapid capacity decay;[7-9] For the lithium anode, the uncontrollable growth of lithium "dendrites" on the surface of lithium metal induces a series of adverse effects, such as the evolution of "dead" lithium, unstable solid electrolyte interphase (SEI), increased polarization and even explosion hazards.[10, 11] Due to the disparate reaction mechanism and different physicochemical characteristics of the sulfur cathode and the lithium anode, synchronously suppressing the shuttle effect and the dendrite growth during long-term cycling has become a formidable technical challenge for the practical application of Li-S batteries.

To date, several approaches have been developed to address these issues, including designing cathode host materials,[12, 13] inserting interlayer,[14] substituting binders[15] and modifying the separator or the lithium anode.[16-19] The majority of these technical strategies only focus on one part of the cell. Adopting an integrated approach that can simultaneously solve the lithium dendrites and Li_2S_x shuttle effect maybe the way forward to make Li-S batteries achieve the commercial realization. Separators, as the essential medium directly contacting and interacting with both the anode and the cathode, play a vital role in the battery system.[20-23] Functionalizing both sides of commercially available separators is considered to be a facile/effective strategy in controlling the interfacial reactions of both the multielectron conversion of sulfur/polysulfide and the lithium deposition/dissolution, further boosting the overall battery performance.[24-26] For this purpose, some asymmetric separator structures have been developed recently to satisfy the distinct requirements of both the cathode and the anode sides.[20, 27, 28] However, the majority of these separators has shown difficulties to maintain the inherent pore structures of the separator itself during the charging/discharging process, representing a constraint for the high-flux Li^+ diffusion.[20, 29] In addition, the complicated design of the asymmetrical separator inevitably increases the difficulty for the separator commercialization. Based on the above analysis, it would be appealing to rationally select and design a multifunctional material using for separator modification, which could simultaneously meet distinct demands of the anode and cathode in Li-S batteries as well as guarantee the smooth ion diffusion.

Vanadium disulfide (VS_2) is one of the transition-metal dichalcogenides (TMDs) that has attracted increasing interests in the fields of electrochemical energy storage in recent years because of its unique chemical/physical characteristics, intrinsic metallic behavior and two-dimensional (2D) layered structure.[30-32] Cui *et al.*[30] have reported that commercial VS_2 could exhibit higher capacity and better cycling stability compared with other TMDs materials (TiS_2, CoS_2, Ni_3S_2, SnS_2 and FeS) and graphite when used as the cathode host material in Li-S batteries. They attributed the performance enhancement to the high conductivity, strong interaction with Li_2S_x, easy Li-ion transport and excellent catalyzing reduction/oxidation capability of VS_2. All these superiorities signify that VS_2 deserves specific attention as a promising functional material not only for the cathode but also as a modifier for the separator, an area which hardly been investigated in the literature. Furthermore, the performance of VS_2 at the anode side, particularly the interaction at the anode/separator interfaces remain unexplored, despite the clear physical advantageous. Also, coating VS_2 on the separators is a more simple and low-cost binder-free modification strategy than coating the lithium metal surface. The facile coating process on the polymer separator would facilitate the practical application and commercial production of Li-S batteries.[33, 34]

Herein, a recyclable VS_2 hexagonal nanotowers (HVS) double-side-modified commercial polypropylene (PP) separator (D-HVS@PP separator) was fabricated *via* a single-step hydrothermal method and subsequent vacuum filtration (Figure S1). The fabricated D-HVS@PP separator kept both the “sulfiphilic” and “lithiophilic” features, which can simultaneously trap Li_2S_x and suppress lithium dendrites. In addition, due to the hexagonal tower-form nanostructure of the HVS, the D-HVS@PP separator also exhibited a high-flux lithium-ion diffusion with improved mechanical strength. As a result, the elaborate separator delivered high charge/discharge capacity and stable cycling performance in Li-S batteries, even under high sulfur loading/lean-electrolyte conditions with the controlled N/P ratio and when used in the pouch Li-S and lithium metal battery systems.

RESULTS AND DISCUSSION

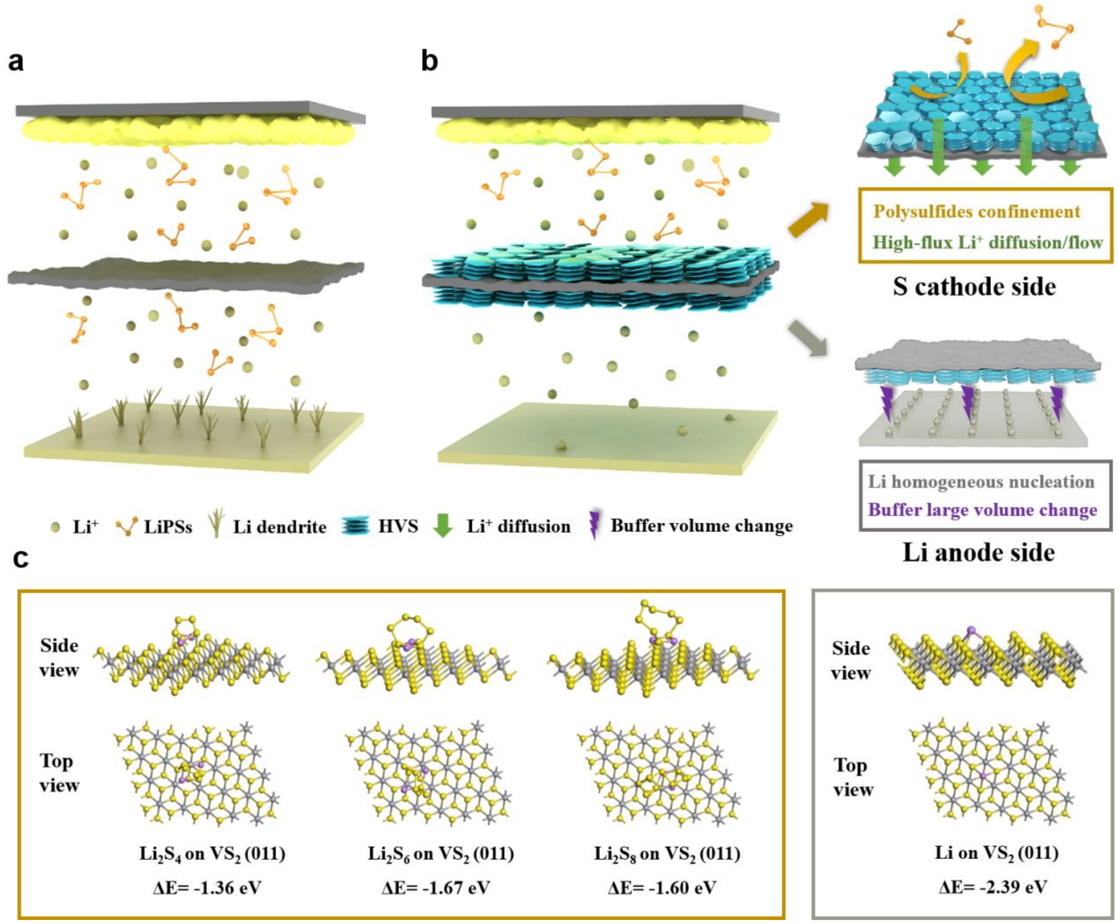

Figure 1. Working mechanism and theory simulation. Schematic illustrations of the working principle of the Li-S battery with (a) PP and (b) D-HVS@PP separator. (c) Density functional theory (DFT) calculation of the absorption energies of Li_2S_4, Li_2S_6, Li_2S_8 and Li on VS_2 (011) facet (Vienna *Ab-initio* Simulation Package (VASP)).

As illustrated in Figure 1, the commonly employed PP separator in conventional Li-S batteries guarantees the primary functions for the efficient migration of lithium ions and the isolation of the counter electrodes. However, it can hardly restrain the polysulfide shuttle, and Li dendrites growth (Figure 1a).[16, 24] In the current work, an "amphiphilic" HVS material was introduced onto both sides of the PP separator, simultaneously realizing the distinct functionalities for the anode and cathode (Figure 1b). In the sulfur cathode side, the HVS can effectively prevent the shuttled Li_2S_x from passing through the separator due to the strong chemical interactions. The designed layer-by-layer stacked nanostructure of the HVS also creates the abundant channels and spaces for high-flux ion diffusion/flow and provides enough exposed active sites for polysulfide adsorption. In addition, the intrinsic metallic nature of the HVS can further reduce the interfacial resistance between the electrode and the separator, enabling low polarization and fast sulfur conversion kinetics[35]. In the lithium anode side, the strong lithiophilic ability and high electronic conductivity of the HVS can induce ions/electrons to uniformly distribute at anode/separator interfaces, avoiding the formation of lithium dendrites caused by the local charge concentration.[36-38] At the same time, the stable hexagonal tower-shaped architecture of the HVS is also beneficial to buffer the large volume change of lithium metal under deep cycling and serves as a physical shield to resist the lithium dendrites growth.[18, 39] Hence, the D-HVS@PP separator can boost an obvious enhancement in battery performance, and the detailed reasons have been analyzed and discussed in the following sections.

The growth process and structural characterizations of the HVS were investigated in Figure S2-6. Firstly, the scanning electron microscopy (SEM) images at various stages of the hydrothermal process are displayed in Figure S2, where the possible formation mechanism of the VS_2 hexagonal nanotowers is also schematically illustrated. PVP, as a surfactant, is playing a crucial role with dual functions of the hexagonal tower-shaped nanostructure.[40] First, it serves as a linking agent to bridge adjacent VS_2 nanoflakes together, leading to the self-assembly of the nanoflake subunits along the c-axis. Second, it plays a vital role on controlling the size and morphology of each VS_2 nanoflake along the ab-plane, leading to the formation of a perfect hexagonal nanostructure instead of the conventional VS_2 microflowers (MVS).[32, 41, 42] The high-resolution transmission electron microscopy (HRTEM), X-ray diffraction (XRD) and X-ray photoelectron spectroscopy (XPS) analysis in Figure S3-5, showed that both HVS and MVS samples possessed the same crystalline phase (JCPDS No. 89-1640), valence state and chemical composition, belonging to the typical VS_2 structure. However, the higher intensity of the XRD peaks and the perfect interlayer structure appears in the HRTEM images suggests that HVS is of longer crystalline order. The HVS exhibited a Brunauer-Emmett-Teller (BET) surface area of 31.4 m^2 g^{-1}, which is over 5 times higher than the MVS (5.8 m^2 g^{-1}), since the multi-layered tower-like nanostructure was conducive to the exposure of more micro/mesopores (10~70 Å) (Figure S6). The higher surface area allows the separator to store more electrolyte and contribute more active sites, facilitating high-flux lithium-ion diffusion and efficient interfacial reactions.[43, 44]

In addition, to evaluate the amphiphilic functional property of the HVS separator, the absorption energies of VS_2 (011) main facet towards the soluble Li_2S_x and metallic lithium were calculated by density functional theory (DFT) simulations. As shown in Figure 1c, the binding energies between VS_2 (011) facet and Li_2S_4, Li_2S_6 and Li_2S_8 were -1.36, -1.67 and -1.60 eV, respectively, much higher than that between graphene and Li_2S_4 (-0.56 eV) (Figure S7). This confirmed that VS_2 possesses strong absorption ability for Li_2S_x, especially longer-chained Li_2S_6 and Li_2S_8. Long-chained Li_2S_x are easier to dissolve and shuttle in the electrolyte and result in the rapid capacity decay of Li-S batteries.[7] Notably, VS_2 also showed high chemical affinity (-2.39 eV) for metallic lithium because of the strong interaction between Li and S atoms. This "sulfiphilic" and "lithiophilic" property emphasizes the potential ability of VS_2 to trap Li_2S_x and suppress lithium dendrites simultaneously.

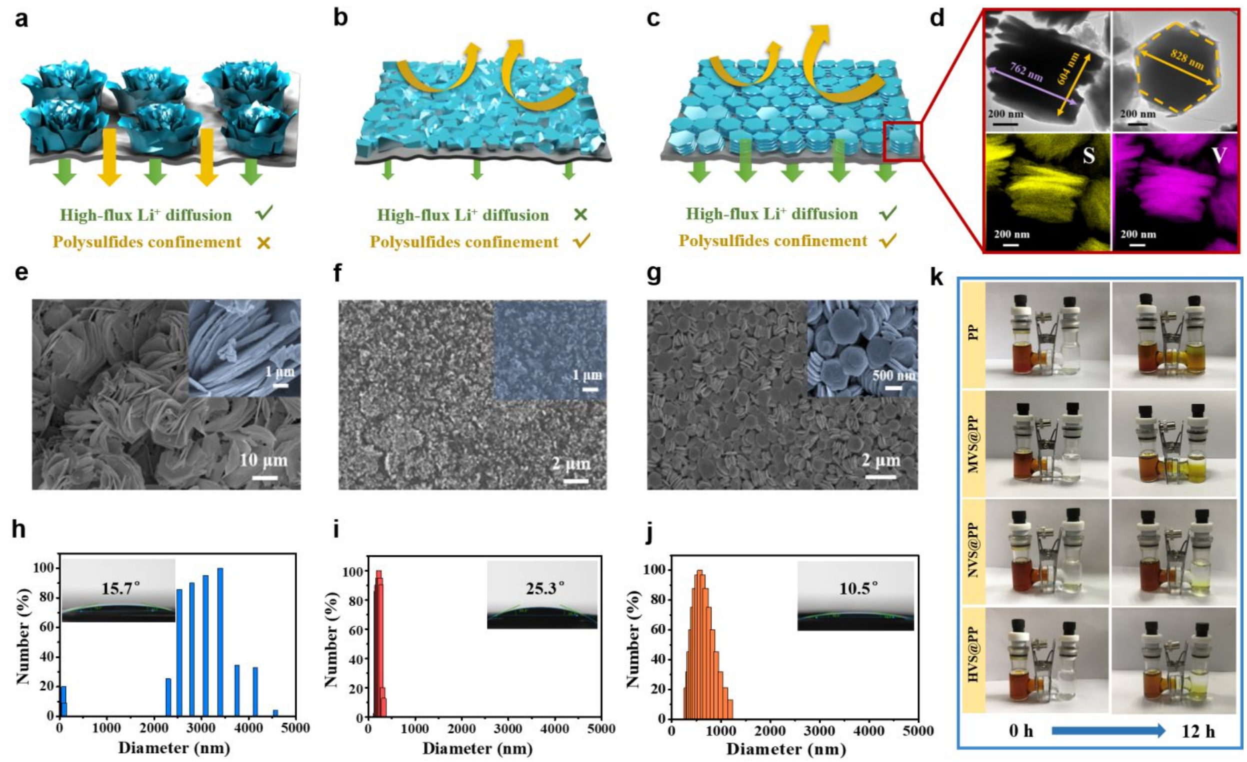

Figure 2. Functional description of different VS_2 modified separators on sulfur cathode side. Functional illustrations of the (a) MVS@PP, (b) NVS@PP and (c) HVS@PP separators on sulfur cathode side. (d) Transmission electron microscopy (TEM) images and element distribution of the VS_2 hexagonal nanotowers. SEM images of (e) MVS@PP, (f) NVS@PP and (g) HVS@PP separators. Particle size distributions and contact angle images (inset) for (h) MVS@PP, (i) NVS@PP and (j) HVS@PP separators, Li-S electrolyte as a test liquid was used in contact angle tests. (k) Diffusion tests of Li_2S_6 with PP, MVS@PP, NVS@PP and HVS@PP separators.

Before verifying the performance of the double-sided treated separator (D-HVS@PP) for the sulfur cathode or the lithium anode, a single-sided HVS@PP separator was first tested to investigate the reactions at one electrode and eliminate the possible influence from counter electrode. Firstly, three different VS_2 modified separators (MVS@PP, VS_2 nano-bulks (NVS)@PP and HVS@PP separators) were compared. As shown in Figure 2a, e and h, the MVS@PP separator is beneficial to achieve high-flux lithium-ion diffusion, due to the high electrolyte affinity of VS_2 itself and the large particle sizes (diameter 2000~5000 nm) of the MVS structure. As a result, the MVS@PP separator exhibited a much smaller contact angle (15.7°) compared with the pure PP separator (37.0°) (Figure S8a). However, the MVS@PP separator can hardly resist the Li_2S_x diffusion because of the large microporous gaps among particles and low surface area of MVS (Figure 2k). Also, the flower-shaped structure and the large particle sizes reduce the contact area between MVS and the PP substrate, leading to the uneven distribution and weak adhesive strength between the components of the MVS@PP (Figure S8b). The second tested separator was NVS@PP (Figure 2b, f, i and k and Figure S9), in which NVS were obtained by directly sonicating the HVS. The NVS particles were less than 500 nm in diameter, which means it could be densely loaded onto the PP separator and effectively suppress Li_2S_x shuttle. However, NVS particles formed a blocking layer on the PP substrate that significantly lowers the electrolyte wettability and hinders the lithium-ion diffusion/flow. For HVS@PP separators, it can be seen that most of the nanotowers are aligned vertically on the separator with the hexagonal layers parallel to the surface (Figure 2g and Figure S10), which may be due to the more stable hexagonal 2D planes and larger plane/height ratio of the as-prepared VS_2 nanotowers.[45, 46] Due to the moderate particle sizes (400~1200 nm), well-designed hexagonal tower-like structure and the high surface area of the HVS, HVS@PP separators (Figure 2c, d, g and j) are able to guarantee the adequate contact area and strong electrostatic interaction for HVS to be tightly linked to the separator (Figure S8b-d).[45, 47] HVS also provided abundant tiny channels on the separator surface for both lithium-ion diffusion/flow and Li_2S_x suppression (Figure 2k).

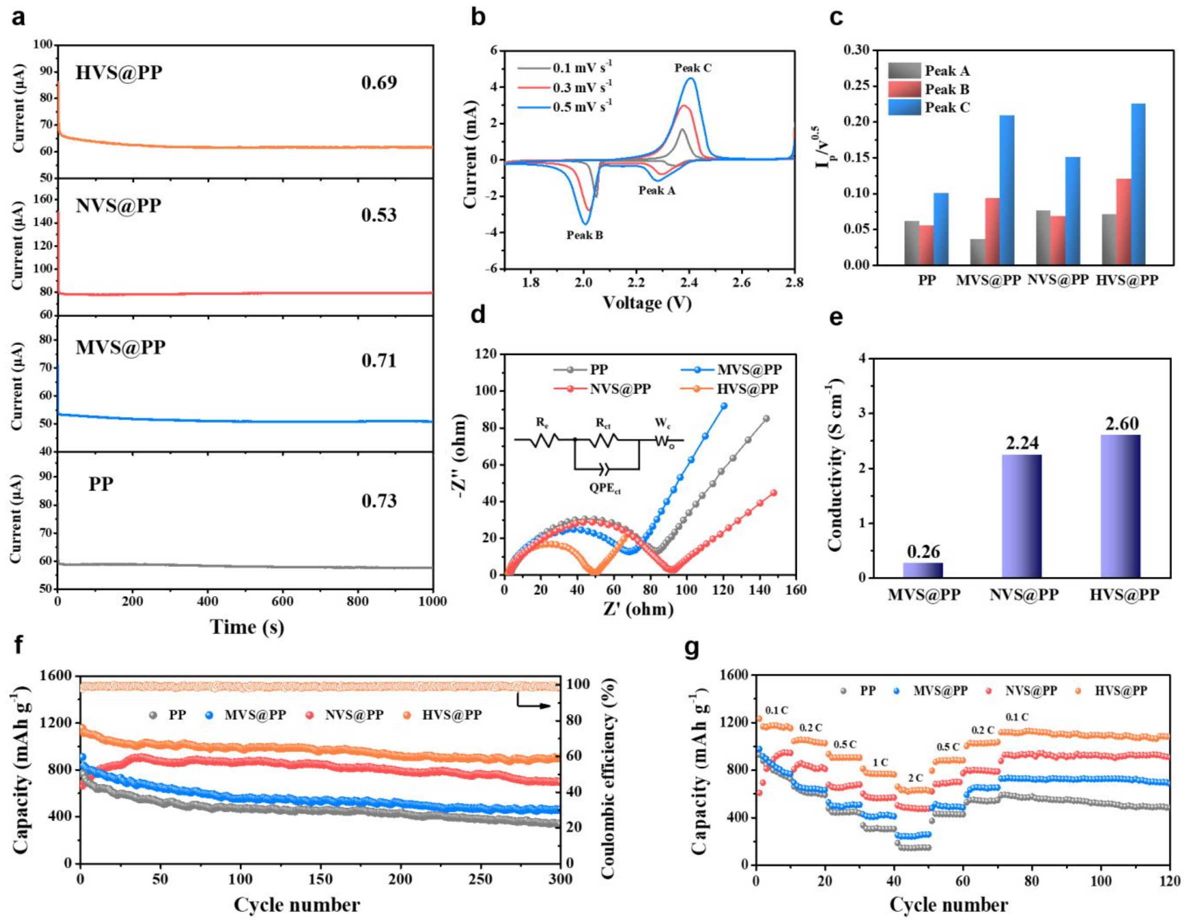

Figure 3. Electrochemical performance towards sulfur cathode side. (a) Lithium-ion transference numbers for the PP, MVS@PP, NVS@PP and HVS@PP separators tested by Li || Li symmetric cells. (b) CV plots of the HVS@PP separator at various scan rates within a potential window of 1.7 V-2.8 V (vs. Li/Li^+). (c) Values of CV peak current (I_p)/square root of the scan rates ($v^{0.5}$) for the four different separators in the first (peak A: $S_8 \rightarrow Li_2S_x$) and second (peak B: $Li_2S_x \rightarrow Li_2S_2/Li_2S$) cathodic reduction processes and the anodic oxidation process (peak C: $Li_2S_2/Li_2S \rightarrow S_8$). (d) EIS curves tested at open-circuit voltage for the four different separators,

inset: equivalent circuit model. (e) Electrical conductivities for the MVS@PP, NVS@PP and HVS@PP separators. (f) Long-term cycling performance of the four different separators at 0.2 C for 300 cycles. (g) Rate performance of the four different separators from 0.1 C to 2 C.

To evaluate the electrochemical performance of various separators towards the sulfur cathode, a series of characterizations were further carried out in a coin-type configuration (Figure 3). Firstly, the lithium-ion transference numbers (t_{Li^+}), defined as the ratio of steady-state current to initial current, of various separators were calculated at a potential of 10 mV.[46] The t_{Li^+} represents the ratio of the total charge carried by lithium ions to that carried by both the lithium ions and the anions in the electrolyte, thus reflecting the lithium-ion transport property of various separators.[48, 49] The t_{Li^+} value of the MVS@PP (0.71) and HVS@PP separators (0.69) are comparable to that of the pure PP separator (0.73). NVS@PP, on the other hand, has the lowest lithium-ion transference numbers (0.53). The low t_{Li^+} value suggesting the dense NVS functional layer covering on the separator surfaces produced a stronger binding for lithium ions, which is unfavorable to lithium-ion transport and conductivity.[46, 49] This is also consistent with the results and previous analysis in Figure 2.

Next, cyclic voltammetry (CV) and electrochemical impedance spectra (EIS) were collected to investigate the lithium-ion transfer rates across various separators. Since fast lithium-ion diffusion facilitates the sulfur conversion kinetics in Li-S battery system, the effective lithium-ion diffusion rates of different VS_2 separators can be acquired by investigating the CV curves at various scan rates. For the CV plots of all the separators (Figure 3b and Figure S11), there are two reduction peaks and one oxidation peaks. The first peak (peak A: ~2.3 V) and the second peak (peak B: ~2.0 V) in the cathodic scan represent the reduction of sulfur to soluble Li_2S_x ($S_8 \rightarrow Li_2S_x$) and the formation of solid lithium sulfides ($Li_2S_x \rightarrow Li_2S_2/Li_2S$). The anodic oxidation peak (peak C: ~2.4 V) corresponds to the reversible transition from lithium sulfides to sulfur ($Li_2S_2/Li_2S \rightarrow S_8$). According to the Randles-Sevcik equation,[30, 50] the peak current (I_p) has a linear relation with the square root of the scan rate ($\nu^{0.5}$) for all separators (Figure S12). The lithium-ion diffusion rate (D_{Li^+}) can be calculated by the slope of the fitted line ($I_p/\nu^{0.5}$). As can be concluded from Figure 3c and Table S1, the VS_2 modified separators at different peaks showed enhanced lithium-ion diffusion rates compared with the pure PP separator. The existed VS_2 at the cathode/separator interfaces accelerates the redox process of insulated lithium sulfides and prevents them from depositing in the voids of the separators, ensuring facile lithium-ion diffusion. Benefiting from the high electrolyte affinity and the abundance of active sites, the HVS@PP separator exhibited the fastest lithium-ion diffusion rates among all the VS_2 modified separators. Notably, the NVS@PP separator displayed the fastest lithium-ion diffusion at peak A, suggesting the efficient reduction from sulfur to Li_2S_x. Nevertheless, it could hardly provide enough sites for the reversible conversion of lithium sulfides because of the dense NVS layer, consequently leading to lower lithium-ion diffusion rate at peaks B and C. The EIS curves of the various separators at open-circuit voltage were further displayed in Figure 3d, where all the Nyquist plots were composed by a high-frequency semicircle and a low-frequency sloped line, attributing to the charge transfer resistance (R_{ct}) and mass-diffusion process, respectively.[44, 51] Based on the fitted equivalent electrical circuit model, the calculated impedance data are summarized in Table S2. The R_{ct} value of the HVS@PP separator (45.8 Ω) was lower than that of the PP (71.7 Ω), MVS@PP (56.3 Ω) and NVS@PP (87.2

Ω) separators. This result verified the faster faradic reaction kinetics and smoother charge transfer of the HVS@PP separator, consistent with the above analysis.[44, 52]

Beside the lithium-ion transference, the conductivity is another vital factor to affect battery performance.[53, 54] The NVS@PP (2.24 S cm^{-1}) and HVS@PP (2.60 S cm^{-1}) separators exhibited an almost tenfold higher surface conductivity compared with the MVS@PP separator (0.26 S cm^{-1}) (Figure 3e), as the microscale flower-shaped structure of MVS could not uniformly distribute on the PP separator surfaces to ensure continuous electron transfer (Figure S8b). It has been proved that a higher surface conductivity of a separator can lower the cathode/separator interfacial resistance, facilitating low polarization (Figure S13) and fast sulfur conversion during charge/discharge processes.[35, 54]

Following the above-detailed analyses on structure and function, the practical cycling performance of various VS_2 modified separators in Li-S batteries was investigated, and the results are shown in Figure 3f. Due to both the fast ion/electron diffusion and effective Li_2S_x suppression, the HVS@PP separator delivered the highest initial discharge capacity of 1156 mAh g^{-1} at 0.2 C (1 C=1675 mAh g^{-1} in Li-S battery). The discharge capacity was maintained at 908 mAh g^{-1} with stabilized Coulombic efficiency (~99 %) and slow capacity attenuation (0.072 % per cycle) after 300 cycles. The NVS@PP separator, on the other hand, exhibited the lowest initial discharge capacity of 665 mAh g^{-1} with a gradual capacity rising in the first 40 cycles derived from the electrochemical activation,[20, 55, 56] due to the dense NVS layer that hindered the lithium-ion diffusion/flow. However, the discharge capacity of the NVS@PP separator was retained at 697 mAh g^{-1} after 300 cycles, higher than that of the MVS@PP (463 mAh g^{-1}) and PP (338 mAh g^{-1})

separators, proving that suppressing Li_2S_x shuttle is more crucial to maintain the stable cycle capacity in Li-S batteries. In addition, the HVS@PP separator also yielded the best rate performance among all separators (Figure 3g). When the current density was increased to 2 C, the HVS@PP separator still delivered a high discharge capacity of 630 mAh g^{-1}, reaffirming the low polarization and the fast reaction kinetics of the HVS@PP separator due to the improved ion/electron transferability at the cathode/separator interface.

A series of post-mortem analyses were further conducted better to evaluate the practical cycling stability of the HVS@PP separator. As shown in Figure S14, the HVS@PP separator still maintained the hexagonal tower-form structure after 300 cycles, proving its high stability in coping with the repeated charging and discharging. EIS plots for the HVS@PP separator after various cycles are also presented in Figure S15, with the corresponding impedance data listed in Table S2. The R_{ct} value of the HVS@PP separator decreased from 45.8 Ω (fresh cell) to 13.5 Ω (after 50 cycles), and 6.3 Ω (after 300 cycles), suggesting a gradually enhanced charge conductivity with the increased number of cycles, which is beneficial to the sulfur redox reaction kinetics in LSBs.[7, 57] The HVS@PP separator also displayed lower R_{ct} values than PP separator after 300 cycles, confirming the superiority of the HVS layer for the fast charge transfer during cycling. Finally, the sulfur content deposited on the lithium metal anodes for the various separators after 300 cycles were quantitatively assessed by inductive coupled plasma-atomic emission spectrometry (ICP-AES) (Figure S16). The lithium metal anode assembled with the HVS@PP separator displayed the lowest sulfur content (5.1 ppm) compared with pure PP, MVS@PP and NVS@PP separators (16.7, 13.4 and 6.7 ppm).

This excellent Li_2S_x suppression ability of the HVS@PP separator once again supports its stable cycling performance shown in Figure 3f.

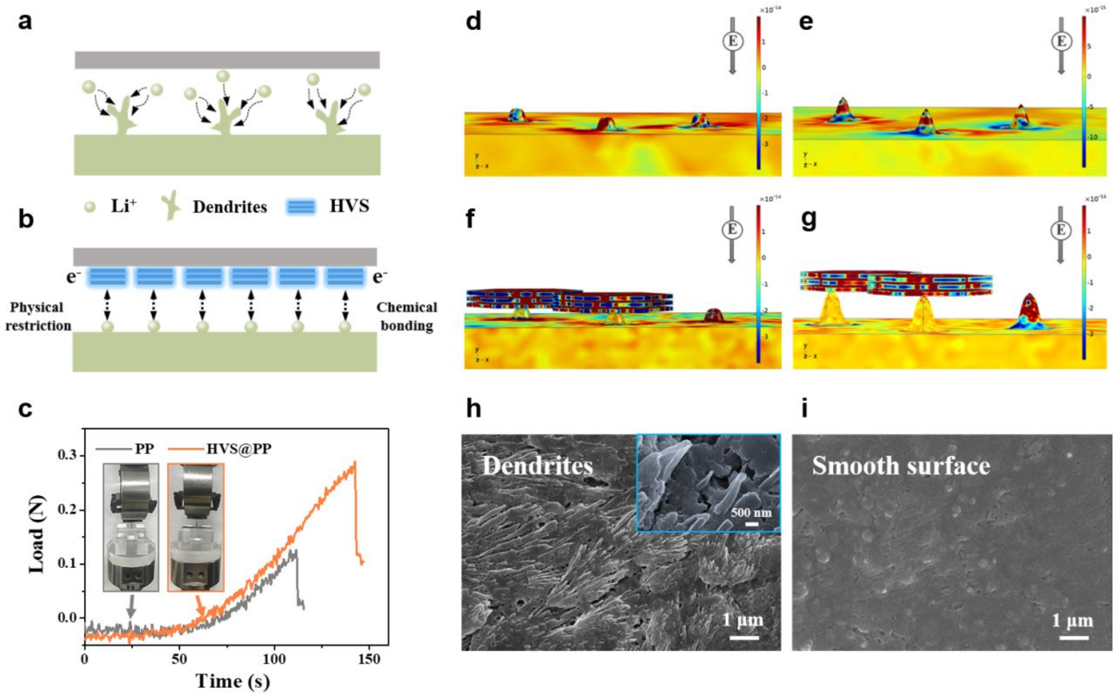

Figure 4. Schematics of lithium growth with different separators on lithium anode side. Functional illustrations of the (a) PP and (b) HVS@PP separators on lithium anode side. (c) Puncture strength tests of the PP and HVS@PP separators, inset: the PP and HVS@PP separators were fixed on a sample holder with a gap width of 8 mm for mechanical puncture tests. Finite element method (FEM) using COMSOL Multiphysics for the simulation of the electric field distribution at different growth periods of (d and e) the lithium dendrites and (f and g) the lithium dendrites covered with the HVS layer. SEM images of the lithium metal anodes with (h) PP and (i) D-HVS@PP separators after stripping/plating for 100 cycles.

Motivated by the excellent performance of the HVS grown on PP (HVS@PP), we then investigated the performance of the double-sided HVS@PP separator for lithium metal anode using various simulation and electrochemical spectroscopic techniques (Figure 4). For clarity, the mechanisms of lithium growth for the three different separators are illustrated schematically. For pure PP separator (Figure 4a), it can hardly cope with both the lithium dendrite growth and the volumetric change of bare lithium metal during repeated stripping/plating cycles. Because of the unevenly distributed charges, lithium ions also tend to aggregate near the dendrites and further accelerate the dendrite growth, leading to a severe consumption of electrolyte and the fragmentation of solid electrolyte interphase (SEI) layer.[11, 58] In contrast, the homogeneous lithium nucleation and growth can be achieved when an HVS layer modifies the surface of the PP separator facing the lithium metal anode for the following reasons (Figure 4b): (a) "Lithiophilic" feature of the HVS (Figure 1c) provides a high chemical affinity with lithium, which can effectively alleviate the dendrite spread and prevent the formation of "dead lithium" during cycling.[36, 59] (b) The stable hexagonal multi-layered nanostructure of the HVS not only accommodate Li deposition and buffers volume expansion of lithium metal during cycling but also improves the puncture resistance of the PP separator to physically resist the lithium dendrite growth (Figure 4c).[18, 24, 39] (c) The improved interfacial conductivity between the separator and the lithium anode ensures homogeneous electric field distribution and decreases the current density, thus conducive to the homogeneous nucleation and the suppression of lithium dendrites growth.[38, 60]

To shed more light on the lithiation process, the COMSOL Multiphysics technique was adopted to simulate the electric field distribution at different growth periods of the lithium dendrites with or without an HVS covering layer (Figure 4d-g and Figure S17).[59, 61] For the bare lithium metal anode, the electric field intensity around the dendrites dramatically increases (visible in red) with the extremely uneven electric field distribution. This demonstrates that lithium ions are more likely to be focused at the formed dendrites due to the tip effect, further leading to the continuous growth of lithium dendrites. Nevertheless, when the lithium dendrites are covered with the conductive HVS layer, the gathered electric fields around the dendrites are dispersed by the multi-layered HVS structure to form a more uniform distribution on the surface of lithium anode. Hence, the tip effect or hotspot around the lithium dendrites is eliminated.

The lithium metal anodes for different separators were further studied after 100 cycles using SEM (Figure 4h and i) and atomic force microscopy (AFM) (Figure S18), to evaluate the practical suppression effect of the D-HVS@PP separator on the lithium dendrites growth. The lithium anode exhibited a quite rough surface with plenty of needle-shaped dendrites when PP separator was used. Conversely, the D-HVS@PP separator maintained a smooth lithium anode surface. The results further confirm the effectiveness of the D-HVS@PP separator in suppressing the dendrite growth as analyzed previously.

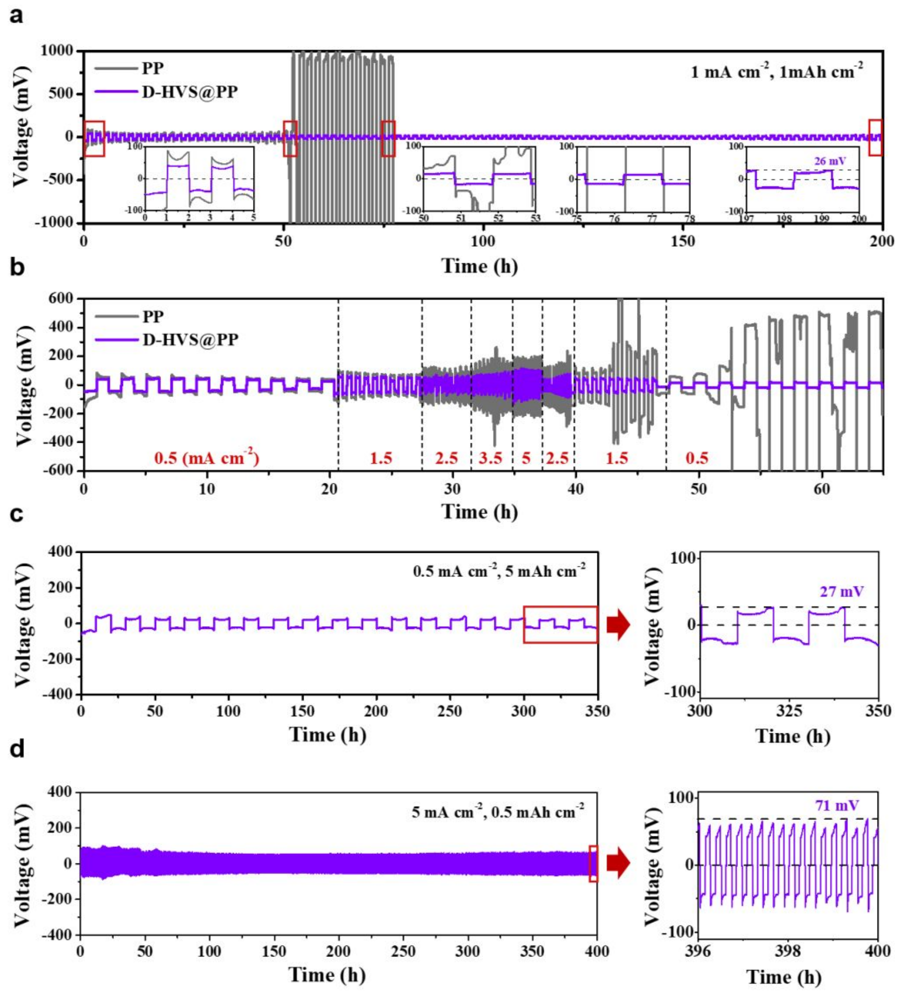

Figure 5. Electrochemical performance towards lithium anode side. (a) The voltage profiles in Li || Li symmetric cells with PP and D-HVS@PP separators at 1 mA cm^{-2} with a stripping/plating capacity of 1 mAh cm^{-2}. (b) Rate performance of the symmetric cells with PP and D-HVS@PP separators at a stripping/plating capacity of 0.5 mAh cm^{-2}. The voltage profiles in Li || Li symmetric cells with D-HVS@PP separator: (c) at 0.5 mA cm^{-2} with a stripping/plating capacity of 5 mAh cm^{-2} and (d) at 5 mA cm^{-2} with a stripping/plating capacity of 0.5 mAh cm^{-2}.

Galvanostatic cycling performances of Li || Li symmetric cells with the PP and D-HVS@PP separators were investigated to evaluate the stability of lithium stripping/plating with different separators (Figure 5). Based on the voltage profiles in Figure 5a, the pure PP separator exhibited an initial overpotential of 89 mV, twice higher than the D-HVS@PP separator (41 mV). In addition, the polarization for the pure PP separator showed a sharp increase to nearly 1000 mV after 50 h, which might be attributed to the excessive formation of 'dead' lithium on the surface of lithium metal resulting in the fragmentation of SEI layer and unstable Li/electrolyte interface accompanying with poor electrical connection.[25, 36] In contrast, the D-HVS@PP separator maintained a flat lithium stripping/plating plateau with a low overpotential of 26 mV even after 200 h. During the switch of different current densities from 0.5 mA cm^{-2} to 5 mA cm^{-2} and reverted to 0.5 mA cm^{-2} (Figure 5b), the D-HVS@PP separator also displayed a more stable polarization vibration compared with the pure PP separator, further indicating its enhanced rate performance in symmetric cells. Even at a larger stripping/plating capacity of 5 mAh cm^{-2} (Figure 5c) or a higher current density of 5 mA cm^{-2} (Figure 5d), the symmetric cells with the D-HVS@PP separator still exhibit stable voltage profiles (~27 mV for 350 h or ~71 mV for 400 h). All the results confirm D-HVS@PP separator can facilitate the uniform lithium nucleation and growth due to the synergistic effect of the effective chemical/physical restriction and the improved interfacial conductivity, subsequently achieving the high cycling stability of lithium metal anode.

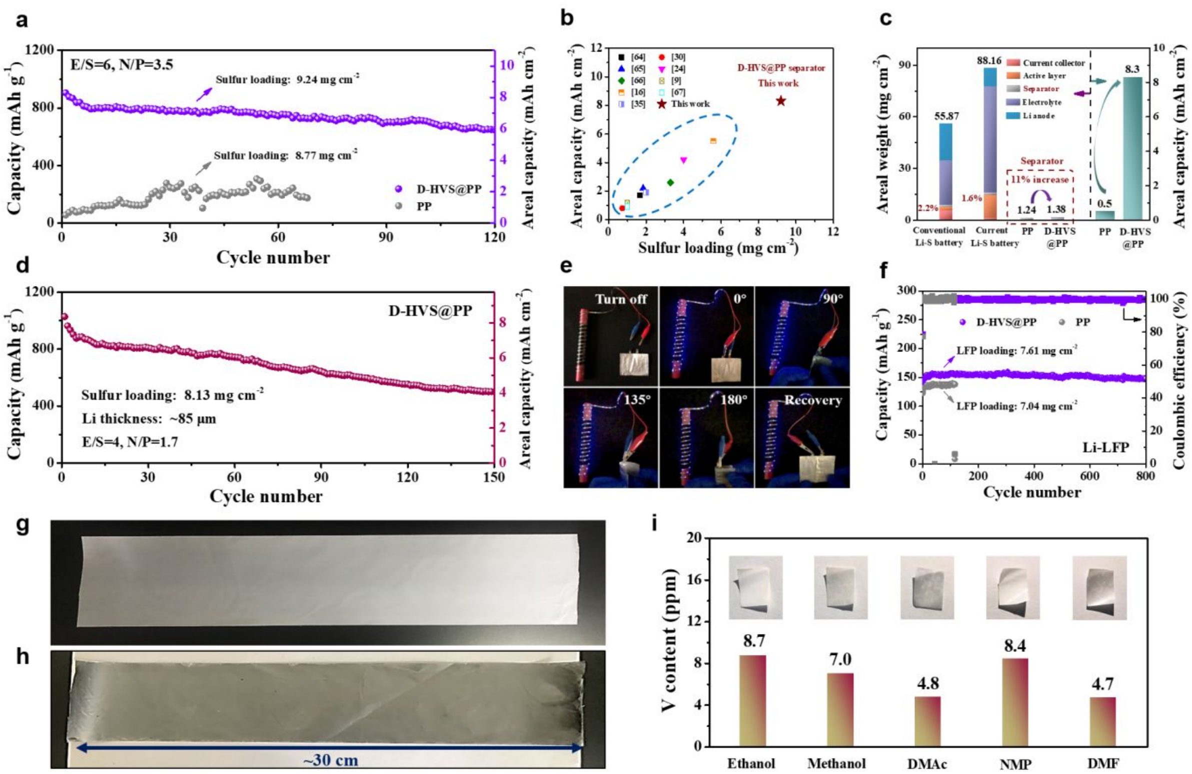

Figure 6. Performance of various battery configurations using different separators. (a) Cycling performance of PP and D-HVS@PP separators under high sulfur-loading and lean-electrolyte conditions at 0.2 C. (b) Comparison of the areal capacities of D-HVS@PP separator at a high sulfur loading with that of other reported similar materials in Li-S battery, more details are shown in Table S4. (c) Comparison of both the areal weight and areal capacity of PP and D-HVS@PP separators. (d) Cycling performance of D-HVS@PP separators under a lower E/S and N/P ratios at 0.2 C (e) LEDs illuminating test by a Li-S pouch cell using the D-HVS@PP separator in various folded states. (f) The cycling performance of PP and D-HVS@PP separators in the Li-$LiFePO_4$ (LFP) batteries. (g) Image of the commercial PP separator. (h) The large-scale fabrication of D-HVS@PP separator. (i) The vanadium content of the various organic solvents (10 mL) after the recycling experiments of D-HVS@PP separator probed by ICP-AES, inset: the corresponding separator photos after the recycling treatment.

Despite numerous efforts made to the development of advanced functional separators, most of the studies focused solely on the high capacity performance and ignored the consideration of sulfur loadings and electrolyte utilization[4, 20]. A low sulfur areal loading (<2.0 mg cm^{-2}) and high electrolyte/sulfur (E/S) ratio (>15 mL g^{-1}) can hardly achieve competitive areal capacities and energy density with that of the state-of-art Li-ion batteries[20]. Accordingly, the D-HVS@PP separator with a high sulfur-loading (9.24 mg cm^{-2}) S/carbon nanofibers (CNFs) cathode and a ~200 μm thick lithium anode (Figure S19a) was employed under a lean-electrolyte condition (6 mL g^{-1}) to explore its potential for practical use. The negative to positive capacity ratio (N/P) for this assembled Li-S battery was calculated to be 3.5 (Table S3).[62, 63] Despite the relatively high polarization, which is due to the improved sulfur loading and the low E/S ratio, the D-HVS@PP separator maintained stable charging/discharging platform and excellent areal capacity of 6.0 mAh cm^{-2} even after 120 cycles. The improved cycle stability can be attributed to the unique amphiphilic property, the high surface conductivity, and the superior electrolyte penetration for Li^+ transfer (Figure 6a and Figure S20). Notably, the D-HVS@PP has achieved an initial capacity of 8.3 mAh cm^{-2}, which is over 16 times higher than the PP separator (0.5 mAh cm^{-2}) under similar conditions. The high initial area capacity and the excellent cyclic stability of the D-HVS@PP separator also outperforms other similarly reported materials applied as separators, cathodes or interlayers in Li-S batteries (Figure 6b and Table S3).[9, 16, 24, 30, 35, 64-67] This performance was achieved just at the expense of an 11% increase in the separator weight (0.14 mg cm^{-2}), accounting for only 0.24% in the basic units of conventional Li-S battery or even lower (0.18%) in the current high sulfur-loading battery system (Figure 6c and Table S5). Furthermore, considering that a thinner

Li anode and a controlled N/P ratio are more relevant to the practical applications of Li-S batteries, the cycling performance of D-HVS@PP separator was further investigated under more strict conditions; *i.e.* with a ~85 μm thick lithium anode (Figure S19b) and the lower N/P (1.7) and E/S (4 mL g^{-1}) ratios (Figure 6d). The battery with D-HVS@PP separator can still deliver a high cell-level gravimetric energy density of 327 Wh kg_{cell}^{-1} (the detailed calculations are shown under Table S5) and favourable stability for 150 cycles closed to the battery in Figure 6a. All these results prove the feasibility of the D-HVS@PP separator in practical Li-S cells.

Furthermore, to achieve wider application visibility, we verified the separator stability in flexible devices. A Li-S pouch cell was assembled using S/CNFs cathode, D-HVS@PP separator, ~200 μm thick lithium anode and vacuum-sealed aluminium-plastic film, with an E/S ratio of 6 mL g^{-1} and an N/P ratio of 3.4. The flexible battery was directly applied in practical light-emitting diodes (LEDs) illumination tests without any additional pressure effect (Figure 6e). This pouch cell exhibited a high open-circuit voltage of 2.45 V with low self-discharge (Figure S21), and can steadily power an array of LEDs in various folded states from 0° (flattened) to 180° (folded) and back to 0° (flattened), and even when repeatedly bent (Movie S1). Apart from the Li-S battery system, the D-HVS@PP separator can also be extended to apply in the Li-$LiFePO_4$ (LFP) batteries assembled with an LFP cathode and a lithium metal anode (Figure 6f). Due to the high charge conductivity, high electrolyte affinity and homogeneous lithium nucleation, the Li-LFP battery with D-HVS@PP separator can deliver a stable discharge capacity of 148.1 mAh g^{-1} and areal capacity of 1.13 mAh cm^{-2} at 1 C (1 C=170 mAh g^{-1} for LFP cathode) even after 800 cycles. These values are higher than that recorded for the conventional PP separator (138.2 mAh g^{-1} and 0.97 mAh cm^{-2}, short circuit after 100 cycles), further highlighting the potential of the D-HVS@PP separator in broader application fields. Notably, compared with the performance for Li-S batteries in Figure 6a and d, the lower but more stable cycling performance of Li-LFP battery is attributed to the distinct insertion/extraction lithium storage mechanism of $LiFePO_4$ cathode and its well-known high stability benefiting from the strong support of phosphate group in its lattice structure.

In addition to the universality, the large-scale fabrication and the recyclability of functional materials are other significant factors for practical and commercially viable separator materials. The D-HVS@PP separator can be simply prepared by one-step hydrothermal technique followed by vacuum filtration, hence easy to be commercialized and applied in the mass production of the D-HVS@PP separator. To further proof, we have prepared a thirty-centimetre-long D-HVS@PP separator through a large-area continuous filtration method (Figure 6g and h). Moreover, considering the cost and toxicity of VS_2 materials,[68] recycling tests were also carried out with the D-HVS@PP separator in various common organic solvents (Figure 6i). The HVS functional materials could be utterly separated from the PP separator to ethanol solvent with an assisted physical vibration, which may be attributed to the higher wettability of ethanol solvent towards PP separator. The recycled vanadium solution can be applied to the reproduction of the D-HVS@PP separator or some other aspects.

CONCLUSIONS

We designed a double-faces separator based on coating commercial PP membrane with 2D HVS (D-HVS@PP) *via* a facile and easy to scale up strategy to simultaneously solve different kinds of problems for the practicality of Li-S batteries. The prepared separator was subjected to a comprehensive characterization program combining with the DFT calculation and COMSOL Multiphysics simulation. The materials spectroscopic and computational characterization confirmed the excellent physical, chemical, and electrochemical properties of the D-HVS@PP when used as a separator in Li-S batteries, *e.g.* the "amphiphilic" nature for both Li_2S_x and pure lithium, high electronic conductivity and special hexagonal tower-like nanostructure. For the sulfur cathode, the HVS functional layer effectively suppressed the Li_2S_x shuttle and ensured the fast interfacial electron transfer and the smooth lithium-ion diffusion through the separator. For the lithium anode, it also promoted the uniform nucleation and growth of lithium and buffered the volume expansion of lithium metal during repeated stripping/plating process. Hence, compared with conventional PP separators, the D-HVS@PP separators enabled a high cell-level gravimetric energy density of 327 Wh kg_{cell}^{-1} with stable cycling even under the practically relevant conditions of high sulfur loading, lean-electrolyte and low N/P ratio, or when applied in flexible Li-S pouch and Li-LFP batteries. In particular, the large-scale fabrication and recyclability of the D-HVS@PP separators are also evaluated to highlight its practicality further. We expect this feasible and straightforward separator design can arouse more attention and thoughts to boost the future commercialized development of the Li-S batteries and even other advanced energy storage technologies.

EXPERIMENTAL SECTION

Chemicals and materials. All chemicals were of analytical grade and used without further purification. Sodium metavanadate ($NaVO_3$), sublimed sulfur (S) and N-methyl-2-pyrrolidone (NMP) were obtained from Aladdin. Thioacetamide (TAA) and ammonium hydroxide ($NH_3 \cdot H_2O$) were purchased from Sinopharm Chemical Reagent Co. Ltd. Polyvinylidene fluoride

(PVDF) was obtained from Arkema. Lithium sulfide (Li_2S) was purchased from Sigma-Aldrich. Poly(vinylpyrrolidone) (PVP K90) was supplied by BASF chemical company in Germany.

Preparation of the VS_2 hexagonal nanotowers (HVS). HVS was prepared using a one-step hydrothermal technique. Firstly, 0.468 g $NaVO_3$, 1.503 g TAA, 6 ml $NH_3 \cdot H_2O$ and 30 ml distilled water were mixed and magnetically stirred for 5 min. Secondly, 1 g PVP K90 was added into the mixture; then the solution was stirred for another 40 min at ambient temperature. The formed precursor solution was then transferred into a 50 ml Teflon-lined stainless-steel autoclave and maintained at 180 °C for 10 h. After cooling, the precipitate was collected and washed thoroughly with water and ethanol several times to recover the final HVS samples.

Preparation of the VS_2 microflowers (MVS) and VS_2 nano-bulks (NVS). MVS and NVS samples were prepared for comparison. Conventional MVS were synthesized using the same synthesis method as the HVS without the addition of PVP K90. NVS were obtained by sonicating the as-prepared HVS in ethanol solution for 1 hour.

Preparation of the HVS@PP, MVS@PP and NVS@PP separators. The VS_2 modified separators were prepared by direct vacuum filtration technology without using any binder. 2 mg of the as-prepared sample (HVS, MVS or NVS) was dispersed in 20 ml ethanol. The resulting suspensions were directly vacuum filtered onto a commercial PP separator and then dried at 60 °C in a vacuum oven for 6 hours, to form the targeted HVS@PP, MVS@PP and NVS@PP separators, respectively.

Preparation of the sulfur cathodes. The sulfur slurry was prepared by ball-milling a mixture of 280 mg sulfur powder, 80 mg Super P, 40 mg PVDF and 1.8 ml N-methyl-pyrrolidone (NMP) for over 6 hours. The slurry was then coated to an aluminum foil and dried under vacuum at 60 ^{o}C for 12 hours to form the sulfur cathode. The sulfur mass loading is ~1.5 mg cm^{-2}.

Preparation of the Li_2S_6 solution. 0.005 M Li_2S_6 solution (30 mM in sulfur) was obtained by chemically reacting sulfur powder with Li_2S in 1,3-dioxolane/1,2-dimethoxyethane solution (DOL/DME, 1:1 by volume).

Characterization. Morphological data and energy dispersive spectra (EDS) mapping were obtained using a field emission scanning electron microscopy (FE-SEM) (GeminiSEM500, China) and a transmission electron microscopy (TEM) (JEOL JEM2100, Japan). X-ray diffraction (XRD) measurements were carried out using a PANalytical X'pert MPDPro (Netherlands) diffractometer with a Cu Ka radiation source (40 kV, 40 mA). Brunauer–Emmett–Teller (BET) surface areas and pore size distributions were obtained at -196 ^oC liquid nitrogen temperature) using an ASAP 2020 (America) instrument. X-ray photoelectron spectroscopy (XPS) measurements were carried out on a Kratos Axis Ultra (England) instrument using a monochromatic Al Ka radiation source (150 W, 15 kV and 1486.6 eV) at 10^{-9} Torr pressure. The contact angle images were obtained on a KRUSS DSA100 (Germany) instrument using Li-S electrolyte as a test liquid. The accurate element contents (sulfur and vanadium) were acquired with an inductively coupled plasma-atomic emission spectrometry (ICP-AES) (Shimadzu ICPE-9000, Japan). The electric conductivities of various VS_2 modified separators were measured on a four-point probe tester (2182A, America) with a testing current from 4 to 8 mA. Mechanical puncture tests of the separators were carried out on an Instron 5548 (America) Micro Tester Load Test Machine, where a lab-made sample holder with a gap width of 8 mm was used to fix the tested separators, and the rate of compression displacement was set to be 1 mm min^{-1}. A SOLVER NEXT (China) atomic Force Microscopy (AFM) was used to study the dendrite growth on the lithium anode surfaces.

Cell assembly and electrochemical measurements. Coin-type (2032) and pouch cells were assembled in an Ar-filled glovebox (DELLIX LS750S, China) with moisture and oxygen contents below 1.0 ppm. For the Li-S batteries, the sulfur cathode and lithium-metal foil anode were separated by various VS_2 modified PP separators. The electrolyte was composed of 1.0 M lithium bis (tri*fl*uoromethanesulfonyl) imide (LITFSI) in a solvent mixture of DME/DOL (1 : 1 by volume) with 1.0 % $LiNO_3$ additive. The quantity of electrolyte was controlled at 10~15 μL per 1 mg sulfur. Galvanostatic charge/discharge tests were carried out using a LANHE battery tester within a voltage window of 1.7~2.8 V (vs. Li/Li^+). Cyclic voltammetry (CV) was performed using a CHI 660D (China) electrochemical workstation in a voltage range of 1.7~2.8 V. Electrochemical impedance spectra (EIS) were obtained in a frequency range from 0.01 Hz to 100 kHz. In addition, the Li || Li symmetric cells were assembled with the various separators sandwiched between two lithium electrodes. The Li-LFP coin-type batteries were constituted by sandwiching separators between an LFP cathode and a ~200 μm thick lithium anode. The electrolyte was 1.0 M $LiPF_6$ in a solution of the ethylene carbonate and diethyl carbonate (1:1 by weight).

Computational method. The density functional theory (DFT) calculation was performed using the Vienna *Ab-initio* Simulation Package.[69, 70] The electron-ion interaction was described by projector augmented-wave (PAW) pseudopotentials. For the exchange and correlation functionals, we use the Perdew-Burke-Ernzerhof (PBE) version of the generalized gradient approximation (GGA) exchange-correlation.[70] In the DFT calculation, the (011) phase of VS_2 and the pure graphene were used to reveal the binding energy with polysulfide (*e.g.* Li_2S_4, Li_2S_6 and Li_2S_8). The vacuum layer thickness was set to 15 Å to avoid virtual interaction and obtain more accurate results. The energy cutoff of 400 eV was used for the wave functions expansion.

The Brillouin zone integration was sampled with a 3 × 3 × 1 k-grid mesh for geometry optimization, and 5 × 5 × 1 k-grid mesh for electronic properties calculations to achieve high accuracy. The energy and force converged to 1.0×10^{-5} eV $atom^{-1}$ and 0.03 $eV \cdot Å^{-1}$. The corresponding binding energy (ΔE_{BE}) is defined as:

$$\Delta E_{BE} = E_{A+B} - E_A - E_B \quad (1)$$

Where the E_{A+B} is the total energy of the structure of the VS_2 (011) or graphene combined with polysulfide, E_A is the total energy of the (011) phase of VS_2 or pure graphene, and E_B is the total energy of the polysulfide (*e.g.* Li_2S_4, Li_2S_6 or Li_2S_8). Based on the definition, a more negative value indicates a stronger binding system.

Finite element method (FEM) simulation. The electric field distribution in different growth periods of the lithium dendrites covered with or without the HVS layer was performed on a three-dimensional (3D) view by COMSOL Multiphysics 5.3a software. The constructed models referring to size ratio, shape and distribution of materials were established by SolidWorks 2016 according to the experimental characterization results, to make the simulation process as close as possible to the actual situation. To simplify the module process, the physics module of "Electric Current Field" under steady-state conditions was used in the subsequent simulation. The simulated electric field intensity was set to be near platform voltage of 2 V with the direction from the separator to the anode. The relative dielectric constant of VS_2 was set to 3.1, and the conductivity of VS_2 was 500 S m^{-1}.[71] The physical field-controlled grids were selected to be the sequence type and extremely refined cell size.

ASSOCIATED CONTENT

Supporting Information

The Supporting Information is available free of charge on the ACS Publications website at DOI: Figures S1 and S2 show the synthetic route and growth mechanism for the HVS. Figures S3-21 show the material characterizations (SEM, TEM, XRD, XPS, AFM and ICP-AES), optical images, electrochemical characterizations, calculations and simulations for various samples. Tables S1-4 show some calculated electrochemical performance parameters for various separators in Li-S batteries, including the lithium-ion diffusion rate, EIS resistance, N/P ratio, areal capacity and areal weight.

Financial Interest Statements

The authors declare no conflict of financial interest.

AUTHOR INFORMATION

Corresponding Author

*E-mail: dingsj@xjtu.edu.cn (S. Ding).

*E-mail: yanwei@xjtu.edu.cn (W. Yan).

*E-mail: kx210@cam.ac.uk (K. Xi)

Author Contributions

J. Wang, K. Xi, W. Yan and S. Ding conceived and designed the work; J. Wang, S. Yi, J. Liu, S. Sun, Y. Liu, D. Yang and G. Gao performed the experiments, characterizations, calculations and simulations; J. Wang and K. Xi wrote the manuscript; J. Wang, K. Xi, A. Abdelkader, W. Yan, S. Ding and R. V. Kumar analyzed the data and revised the manuscript. All authors have given approval to the final version of the manuscript.

ACKNOWLEDGMENTS

This work was supported by the Natural Science Foundation of China (No. 51803164; 51773165), China Postdoctoral Science Foundation (2018M643635), Natural Science

Foundation of Shaanxi Province (2019JQ-126) and Young Talent Support Plan of Xi'an Jiaotong University. The authors thank Zijun Ren and Chao Li at Instrument Analysis Center of Xi'an Jiaotong University for their assistance with SEM and TEM analysis.

REFERENCES

1. Griffith, K. J.; Wiaderek, K. M.; Cibin, G.; Marbella, L. E.; Grey, C. P. Niobium Tungsten Oxides for High-Rate Lithium-Ion Energy Storage. *Nature* **2018**, *559*, 556-563.

2. Cha, E.; Patel, M. D.; Park, J.; Hwang, J.; Prasad, V.; Cho, K.; Choi, W. 2D MoS_2 as an Efficient Protective Layer for Lithium Metal Anodes in High-Performance Li-S Batteries. *Nat. Nanotechnol.* **2018**, *13*, 337-344.

3. Zhang, M.; Xiang, L.; Galluzzi, M.; Jiang, C.; Zhang, S.; Li, J.; Tang, Y. Uniform Distribution of Alloying/Dealloying Stress for High Structural Stability of an Al Anode in High-Areal-Density Lithium-Ion Batteries. *Adv. Mater.* **2019**, *31*, 1900826.

4. Pang, Q.; Shyamsunder, A.; Narayanan, B.; Kwok, C. Y.; Curtiss, L. A.; Nazar, L. F. Tuning the Electrolyte Network Structure to Invoke Quasi-Solid State Sulfur Conversion and Suppress Lithium Dendrite Formation in Li-S Batteries. *Nature Energy* **2018**, *3*, 783-791.

5. Chang, J.; Shang, J.; Sun, Y.; Ono, L. K.; Wang, D.; Ma, Z.; Huang, Q.; Chen, D.; Liu, G.; Cui, Y.; Qi, Y.; Zheng, Z. Flexible and Stable High-Energy Lithium-Sulfur Full Batteries with Only 100% Oversized Lithium. *Nat. Commun.* **2018**, *9*, 4480.

6. Tsao, Y.; Lee, M.; Miller, E. C.; Gao, G.; Park, J.; Chen, S.; Katsumata, T.; Tran, H.; Wang, L.-W.; Toney, M. F.; Cui, Y.; Bao, Z. Designing a Quinone-Based Redox Mediator to Facilitate Li_2S Oxidation in Li-S Batteries. *Joule* **2019**, *3*, 872–884.

7. Wang, J.; Yang, G.; Chen, J.; Liu, Y.; Wang, Y.; Lao, C. Y.; Xi, K.; Yang, D.; Harris, C. J.; Yan, W.; Ding, S.; Kumar, R. V. Flexible and High-Loading Lithium-Sulfur Batteries Enabled by Integrated Three-In-One Fibrous Membranes. *Adv. Energy Mater.* **2019**, *9*, 1902001.

8. Xu, G.; Kushima, A.; Yuan, J.; Dou, H.; Xue, W.; Zhang, X.; Yan, X.; Li, J. Ad Hoc Solid Electrolyte on Acidized Carbon Nanotube Paper Improves Cycle Life of Lithium-Sulfur Batteries. *Energy Environ. Sci.* **2017**, *10*, 2544-2551.

9. Xi, K.; He, D.; Harris, C.; Wang, Y.; Lai, C.; Li, H.; Coxon, P. R.; Ding, S.; Wang, C.; Kumar, R. V. Enhanced Sulfur Transformation by Multifunctional FeS_2/FeS/S Composites for High-Volumetric Capacity Cathodes in Lithium-Sulfur Batteries. *Adv. Sci.* **2019**, *6*, 1800815.

10. Lin, D.; Liu, Y.; Cui, Y. Reviving the Lithium Metal Anode for High-Energy Batteries. *Nat. Nanotechnol.* **2017**, *12*, 194-206.

11. Cheng, X. B.; Zhang, R.; Zhao, C. Z.; Zhang, Q. Toward Safe Lithium Metal Anode in Rechargeable Batteries: A Review. *Chem. Rev.* **2017**, *117*, 10403-10473.

12. Lin, H.; Yang, L.; Jiang, X.; Li, G.; Zhang, T.; Yao, Q.; Zheng, G. W.; Lee, J. Y. Electrocatalysis of Polysulfide Conversion by Sulfur-Deficient MoS_2 Nanoflakes for Lithium-Sulfur Batteries. *Energy Environ. Sci.* **2017**, *10*, 1476-1486.

13. Xi, K.; Chen, B.; Li, H.; Xie, R.; Gao, C.; Zhang, C.; Kumar, R. V.; Robertson, J. Soluble Polysulphide Sorption Using Carbon Nanotube Forest for Enhancing Cycle Performance in a Lithium-Sulphur Battery. *Nano Energy* **2015**, *12*, 538-546.

14. Gu, X.; Wang, Y.; Lai, C.; Qiu, J.; Li, S.; Hou, Y.; Martens, W.; Mahmood, N.; Zhang, S. Microporous Bamboo Biochar for Lithium-Sulfur Batteries. *Nano Res.* **2014**, *8*, 129-139.

15. Chen, H.; Ling, M.; Hencz, L.; Ling, H. Y.; Li, G.; Lin, Z.; Liu, G.; Zhang, S. Exploring Chemical, Mechanical, and Electrical Functionalities of Binders for Advanced Energy-Storage Devices. *Chem. Rev.* **2018**, *118*, 8936-8982.

16. He, J.; Chen, Y.; Manthiram, A. Vertical Co_9S_8 Hollow Nanowall Arrays Grown on a Celgard Separator as a Multifunctional Polysulfide Barrier for High-Performance Li-S Batteries. *Energy Environ. Sci.* **2018**, *11*, 2560-2568.

17. Li, G.; Wang, C.; Cai, W.; Lin, Z.; Li, Z.; Zhang, S. The Dual Actions of Modified Polybenzimidazole in Taming the Polysulfide Shuttle for Long-Life Lithium-Sulfur Batteries. *NPG Asia Mater.* **2016**, *8*, e317-e317.

18. Liu, S.; Xia, X.; Zhong, Y.; Deng, S.; Yao, Z.; Zhang, L.; Cheng, X.-B.; Wang, X.; Zhang, Q.; Tu, J. 3D TiC/C Core/Shell Nanowire Skeleton for Dendrite-Free and Long-Life Lithium Metal Anode. *Adv. Energy Mater.* **2018**, *8*, 1702322.

19. Dong, J.; Dai, H.; Fan, Q.; Lai, C.; Zhang, S. Grain Refining Mechanisms: Initial Levelling Stage During Nucleation for High-Stability Lithium Anodes. *Nano Energy* **2019**, *66*, 104128.

20. Peng, H.-J.; Huang, J.-Q.; Cheng, X.-B.; Zhang, Q. Review on High-Loading and High-Energy Lithium-Sulfur Batteries. *Adv. Energy Mater.* **2017**, *7*, 1700260.

21. Bai, S.; Liu, X.; Zhu, K.; Wu, S.; Zhou, H. Metal-Organic Framework-Based Separator for Lithium-Sulfur Batteries. *Nature Energy* **2016**, *1*, 16094.

22. Lee, Y.-H.; Kim, J.-H.; Kim, J.-H.; Yoo, J.-T.; Lee, S.-Y. Spiderweb-Mimicking Anion-Exchanging Separators for Li-S Batteries. *Adv. Funct. Mater.* **2018**, *28*, 1801422.

23. Chang, Z.; Qiao, Y.; Wang, J.; Deng, H.; He, P.; Zhou, H. Fabricating Better Metal-Organic Frameworks Separators for Li-S Batteries: Pore Sizes Effects Inspired Channel Modification Strategy. *Energy Storage Mater.* **2020**, *25*, 164-171.

24. Wu, J.; Zeng, H.; Li, X.; Xiang, X.; Liao, Y.; Xue, Z.; Ye, Y.; Xie, X. Ultralight Layer-By-Layer Self-Assembled MoS_2-Polymer Modified Separator for Simultaneously Trapping Polysulfides and Suppressing Lithium Dendrites. *Adv. Energy Mater.* **2018**, *8*, 1802430.

25. He, Y.; Chang, Z.; Wu, S.; Qiao, Y.; Bai, S.; Jiang, K.; He, P.; Zhou, H. Simultaneously Inhibiting Lithium Dendrites Growth and Polysulfides Shuttle by a Flexible MOF-Based Membrane in Li-S Batteries. *Adv. Energy Mater.* **2018**, *8*, 1802130.

26. Li, Y. J.; Wang, C.; Wang, W. Y.; Eng, A. Y. S.; Wan, M. T.; Fu, L.; Mao, E. Y.; Li, G. C.; Tang, J.; Seh, Z. W.; Sun, Y. M. Enhanced Chemical Immobilization and Catalytic Conversion of Polysulfide Intermediates Using Metallic Mo Nanoclusters for High-Performance Li-S Batteries. *ACS Nano* **2020**, *14*, 1148-1157.

27. Li, M.; Wan, Y.; Huang, J.-K.; Assen, A. H.; Hsiung, C.-E.; Jiang, H.; Han, Y.; Eddaoudi, M.; Lai, Z.; Ming, J.; Li, L.-J. Metal-Organic Framework-Based Separators for Enhancing Li-S Battery Stability: Mechanism of Mitigating Polysulfide Diffusion. *ACS Energy Lett.* **2017**, *2*, 2362-2367.

28. Kim, J.-H.; Lee, Y.-H.; Cho, S.-J.; Gwon, J.-G.; Cho, H.-J.; Jang, M.; Lee, S.-Y.; Lee, S.-Y. Nanomat Li-S Batteries Based on All-Fibrous Cathode/Separator Assemblies and Reinforced Li Metal Anodes: Towards Ultrahigh Energy Density and Flexibility. *Energy Environ. Sci.* **2019**, *12*, 177-186.

29. Pan, Y.; Chou, S.; Liu, H. K.; Dou, S. X. Functional Membrane Separators for Next-Generation High-Energy Rechargeable Batteries. *Natl. Sci. Rev.* **2017**, *4*, 917-933.

30. Zhou, G.; Tian, H.; Jin, Y.; Tao, X.; Liu, B.; Zhang, R.; Seh, Z. W.; Zhuo, D.; Liu, Y.; Sun, J.; Zhao, J.; Zu, C.; Wu, D. S.; Zhang, Q.; Cui, Y. Catalytic Oxidation of Li_2S on the Surface of Metal Sulfides for Li-S Batteries. *P. Natl. Acad. Sci.* **2017**, *114*, 840-845.

31. Chen, X.; Peng, H.-J.; Zhang, R.; Hou, T.-Z.; Huang, J.-Q.; Li, B.; Zhang, Q. An Analogous Periodic Law for Strong Anchoring of Polysulfides on Polar Hosts in Lithium Sulfur Batteries: S- or Li-Binding on First-Row Transition-Metal Sulfides? *ACS Energy Lett.* **2017**, *2*, 795-801.

32. Sun, R.; Wei, Q.; Sheng, J.; Shi, C.; An, Q.; Liu, S.; Mai, L. Novel Layer-By-Layer Stacked VS_2 Nanosheets with Intercalation Pseudocapacitance for High-Rate Sodium Ion Charge Storage. *Nano Energy* **2017**, *35*, 396-404.

33. Yan, J.; Liu, F.; Hu, Z.; Gao, J.; Zhou, W.; Huo, H.; Zhou, J.; Li, L. Realizing Dendrite-Free Lithium Deposition with a Composite Separator. *Nano Lett.* **2020**, *20*, 3798-3807.

34. Fu, C.; Venturi, V.; Kim, J.; Ahmad, Z.; Ells, A. W.; Viswanathan, V.; Helms, B. A. Universal Chemomechanical Design Rules for Solid-Ion Conductors to Prevent Dendrite Formation in Lithium Metal Batteries. *Nat. Mater.* **2020**, DOI: 10.1038/s41563-020-0655-2.

35. Sun, J.; Sun, Y.; Pasta, M.; Zhou, G.; Li, Y.; Liu, W.; Xiong, F.; Cui, Y. Entrapment of Polysulfides by a Black-Phosphorus-Modified Separator for Lithium-Sulfur Batteries. *Adv. Mater.* **2016**, *28*, 9797-9803.

36. Ye, H.; Zheng, Z. J.; Yao, H. R.; Liu, S. C.; Zuo, T. T.; Wu, X. W.; Yin, Y. X.; Li, N. W.; Gu, J. J.; Cao, F. F.; Guo, Y. G. Guiding Uniform Li Plating/Stripping through Lithium-Aluminum Alloying Medium for Long-Life Li Metal Batteries. *Angew. Chem. Int. Ed.* **2019**, *58*, 1094-1099.

37. Oh, J.; Jo, H.; Lee, H.; Kim, H.-T.; Lee, Y. M.; Ryou, M.-H. Polydopamine-Treated Three-Dimensional Carbon Fiber-Coated Separator for Achieving High-Performance Lithium Metal Batteries. *J. Power Sources* **2019**, *430*, 130-136.

38. Zhang, R.; Cheng, X. B.; Zhao, C. Z.; Peng, H. J.; Shi, J. L.; Huang, J. Q.; Wang, J.; Wei, F.; Zhang, Q. Conductive Nanostructured Scaffolds Render Low Local Current Density to Inhibit Lithium Dendrite Growth. *Adv. Mater.* **2016**, *28*, 2155-2162.

39. Luo, J.; Wang, C.; Wang, H.; Hu, X.; Matios, E.; Lu, X.; Zhang, W.; Tao, X.; Li, W. Pillared Mxene with Ultralarge Interlayer Spacing as a Stable Matrix for High Performance Sodium Metal Anodes. *Adv. Funct. Mater.* **2019**, *29*, 1805946.

40. Koczkur, K. M.; Mourdikoudis, S.; Polavarapu, L.; Skrabalak, S. E. Polyvinylpyrrolidone (PVP) in Nanoparticle Synthesis. *Dalton Trans.* **2015**, *44*, 17883-17905.

41. Fang, Z.; Hao, S.; Long, L.; Fang, H.; Qiang, T.; Song, Y. The Enhanced Photoelectrochemical Response of $SnSe_2$ Nanosheets. *CrystEngComm* **2014**, *16*, 2404.

42. Chen, J. S.; Liu, J.; Qiao, S. Z.; Xu, R.; Lou, X. W. Formation of Large 2D Nanosheets *via* PVP-Assisted Assembly of Anatase TiO_2 Nanomosaics. *Chem. Commun.* **2011**, *47*, 10443-10445.

43. Lai, C.; Wu, Z.; Gu, X.; Wang, C.; Xi, K.; Kumar, R. V.; Zhang, S. Reinforced Conductive Confinement of Sulfur for Robust and High-Performance Lithium-Sulfur Batteries. *ACS Appl. Mater. Interfaces* **2015**, 7, 23885-23892.

44. Shao, H.; Ai, F.; Wang, W.; Zhang, H.; Wang, A.; Feng, W.; Huang, Y. Crab Shell-Derived Nitrogen-Doped Micro-/Mesoporous Carbon as an Effective Separator Coating for High Energy Lithium-Sulfur Batteries. *J. Mater. Chem. A* **2017**, *5*, 19892-19900.

45. Ling, Z.; Ren, C. E.; Zhao, M. Q.; Yang, J.; Giammarco, J. M.; Qiu, J.; Barsoum, M. W.; Gogotsi, Y. Flexible and Conductive Mxene Films and Nanocomposites with High Capacitance. *P. Natl. Acad. Sci.* **2014**, *111*, 16676-16681.

46. Ghazi, Z. A.; He, X.; Khattak, A. M.; Khan, N. A.; Liang, B.; Iqbal, A.; Wang, J.; Sin, H.; Li, L.; Tang, Z. MoS_2/Celgard Separator as Efficient Polysulfide Barrier for Long-Life Lithium-Sulfur Batteries. *Adv. Mater.* **2017**, *29*, 1606817.

47. Zhang, D.; Wang, S.; Li, B.; Gong, Y.; Yang, S. Horizontal Growth of Lithium on Parallelly Aligned Mxene Layers towards Dendrite-Free Metallic Lithium Anodes. *Adv. Mater.* **2019**, *31*, 1901820.

48. Chen, L.; Li, W.; Fan, L. Z.; Nan, C. W.; Zhang, Q. Intercalated Electrolyte with High Transference Number for Dendrite-Free Solid-State Lithium Batteries. *Adv. Funct. Mater.* **2019**, *29*, 1901047.

49. Wang, Z.; Huang, W.; Hua, J.; Wang, Y.; Yi, H.; Zhao, W.; Zhao, Q.; Jia, H.; Fei, B.; Pan, F. An Anionic-MOF-Based Bifunctional Separator for Regulating Lithium Deposition and

Suppressing Polysulfides Shuttle in Li-S Batteries. *Small Methods* **2020**, *DOI: 10.1002/smtd.202000082*, 2000082.

50. Wang, Y.; Zhang, R.; Chen, J.; Wu, H.; Lu, S.; Wang, K.; Li, H.; Harris, C. J.; Xi, K.; Kumar, R. V.; Ding, S. Enhancing Catalytic Activity of Titanium Oxide in Lithium-Sulfur Batteries by Band Engineering. *Adv. Energy Mater.* **2019**, *9*, 1900953.

51. Yu, M.; Wang, Z.; Wang, Y.; Dong, Y.; Qiu, J. Freestanding Flexible Li_2S Paper Electrode with High Mass and Capacity Loading for High-Energy Li-S Batteries. *Adv. Energy Mater.* **2017**, *7*, 1700018.

52. Cherian, C. T.; Sundaramurthy, J.; Reddy, M. V.; Suresh Kumar, P.; Mani, K.; Pliszka, D.; Sow, C. H.; Ramakrishna, S.; Chowdari, B. V. Morphologically Robust $NiFe_2O_4$ Nanofibers as High Capacity Li-Ion Battery Anode Material. *ACS Appl. Mater. Interfaces* **2013**, *5*, 9957.

53. Sun, L.; Wang, D.; Luo, Y.; Wang, K.; Kong, W.; Wu, Y.; Zhang, L.; Jiang, K.; Li, Q.; Zhang, Y.; Wang, J.; Fan, S. Sulfur Embedded in a Mesoporous Carbon Nanotube Network as a Binder-Free Electrode for High-Performance Lithium-Sulfur Batteries. *ACS Nano* **2016**, *10*, 1300-1308.

54. Wang, H.; Zhang, W.; Liu, H.; Guo, Z. A Strategy for Configuration of an Integrated Flexible Sulfur Cathode for High-Performance Lithium-Sulfur Batteries. *Angew. Chem. Int. Ed.* **2016**, *55*, 3992-3996.

55. Wang, J.; Yang, G.; Wang, L.; Yan, W. Synthesis of One-Dimensional $NiFe_2O_4$ Nanostructures: Tunable Morphology and High-Performance Anode Materials for Li Ion Batteries. *J. Mater. Chem. A* **2016**, *4*, 8620-8629.

56. Mao, Y.; Li, G.; Guo, Y.; Li, Z.; Liang, C.; Peng, X.; Lin, Z. Foldable Interpenetrated Metal-Organic Frameworks/Carbon Nanotubes Thin Film for Lithium-Sulfur Batteries. *Nat. Commun.* **2017**, *8*, 14628.

57. Wang, L.; He, Y.-B.; Shen, L.; Lei, D.; Ma, J.; Ye, H.; Shi, K.; Li, B.; Kang, F. Ultra-Small Self-Discharge and Stable Lithium-Sulfur Batteries Achieved by Synergetic Effects of Multicomponent Sandwich-Type Composite Interlayer. *Nano Energy* **2018**, *50*, 367-375.

58. Zhang, R.; Li, N. W.; Cheng, X. B.; Yin, Y. X.; Zhang, Q.; Guo, Y. G. Advanced Micro/Nanostructures for Lithium Metal Anodes. *Adv. Sci.* **2017**, *4*, 1600445.

59. Liu, B.; Zhang, Y.; Pan, G.; Ai, C.; Deng, S.; Liu, S.; Liu, Q.; Wang, X.; Xia, X.; Tu, J. Ordered Lithiophilic Sites to Regulate Li Plating/Stripping Behavior for Superior Lithium Metal Anodes. *J. Mater. Chem. A* **2019**, *7*, 21794-21801.

60. Cheng, X.-B.; Peng, H.-J.; Huang, J.-Q.; Zhang, R.; Zhao, C.-Z.; Zhang, Q. Dual-Phase Lithium Metal Anode Containing a Polysulfide-Induced Solid Electrolyte Interphase and Nanostructured Graphene Framework for Lithium-Sulfur Batteries. *ACS Nano* **2015**, *9*, 6373-6382.

61. Wang, A.; Deng, Q.; Deng, L.; Guan, X.; Luo, J. Eliminating Tip Dendrite Growth by Lorentz Force for Stable Lithium Metal Anodes. *Adv. Funct. Mater.* **2019**, *29*, 1902630.

62. Abe, Y.; Kumagai, S. Effect of Negative/Positive Capacity Ratio on the Rate and Cycling Performances of $LiFePO_4$/Graphite Lithium-Ion Batteries. *J. Energy Storage* **2018**, *19*, 96-102.

63. Lu, K.; Liu, Y.; Chen, J.; Zhang, Z.; Cheng, Y. Redox Catalytic and Quasi-Solid Sulfur Conversion for High-Capacity Lean Lithium Sulfur Batteries. *ACS Nano* **2019**, *13*, 14540-14548.

64. Wu, H.; Huan, Y.; Wang, D.; Li, M.; Cheng, X.; Bai, Z.; Wu, P.; Peng, W.; Zhang, R.; Ji, Z.; Zou, M.; Yan, X. Hierarchical VS_2 Nano-Flowers as Sulfur Host for Lithium Sulfur Battery Cathodes. *J. Electrochem. Soc.* **2019**, *166*, A188-A194.

65. Cheng, Z.; Xiao, Z.; Pan, H.; Wang, S.; Wang, R. Elastic Sandwich-Type RGO-VS_2/S Composites with High Tap Density: Structural and Chemical Cooperativity Enabling Lithium-Sulfur Batteries with High Energy Density. *Adv. Energy Mater.* **2018**, *8*, 1702337.

66. Guo, Y.; Zhang, Y.; Zhang, Y.; Xiang, M.; Wu, H.; Liu, H.; Dou, S. Interwoven V_2O_5 Nanowire/Graphene Nanoscroll Hybrid Assembled as Efficient Polysulfide-Trapping-Conversion Interlayer for Long-Life Lithium-Sulfur Batteries. *J. Mater. Chem. A* **2018**, *6*, 19358-19370.

67. Dong, Y.; Zheng, S.; Qin, J.; Zhao, X.; Shi, H.; Wang, X.; Chen, J.; Wu, Z. S. All-Mxene-Based Integrated Electrode Constructed by Ti_3C_2 Nanoribbon Framework Host and Nanosheet Interlayer for High-Energy-Density Li-S Batteries. *ACS Nano* **2018**, *12*, 2381-2388.

68. Feng, J.; Sun, X.; Wu, C.; Peng, L.; Lin, C.; Hu, S.; Yang, J.; Xie, Y. Metallic Few-Layered VS_2 Ultrathin Nanosheets: High Two-Dimensional Conductivity for In-Plane Supercapacitors. *J. Am. Chem. Soc.* **2011**, *133*, 17832-17838.

69. Kresse, G.; Furthmüller, J. Efficient Iterative Schemes for *Ab Initio* Total-Energy Calculations Using a Plane-Wave Basis Set. *Phys. Rev. B* **1996**, *54*, 11169-11186.

70. Kresse, G.; Hafner, J. *Ab Initio* Molecular-Dynamics Simulation of the Liquid-Metal-Amorphous-Semiconductor Transition in Germanium. *Phys. Rev. B* **1994**, *49*, 14251-14269.

71. Yu, D.; Pang, Q.; Gao, Y.; Wei, Y.; Wang, C.; Chen, G.; Du, F. Hierarchical Flower-Like VS_2 Nanosheets-a High Rate-Capacity and Stable Anode Material for Sodium-Ion Battery. *Energy Storage Mater.* **2018**, *11*, 1-7.

For Table of Contents Use Only

Suppressing the Shuttle Effect and Dendrite Growth in Lithium-Sulfur Batteries